Inorganic Chemistry
Article
pubs.acs.org/IC

Anionogenic Mixed Valency in $K_xBa_{1-x}O_{2-\delta}$

Shivakumara Giriyapura,[†,⊥,∥] Baomin Zhang,[‡,∥] Robert A. de Groot,[†,‡] Gilles A. de Wijs,[‡] Antonio Caretta,[†] Paul H. M. van Loosdrecht,[†,⊗] Winfried Kockelmann,[§] Thomas T. M. Palstra,[†] and Graeme R. Blake*[,†]

[†]Zernike Institute for Advanced Materials, University of Groningen, Nijenborgh 4, 9747 AG Groningen, The Netherlands
[‡]Electronic Structure of Materials, IMM, Radboud University Nijmegen, Heyendaalseweg 135, 6525 AJ Nijmegen, The Netherlands
[§]STFC ISIS Facility, Rutherford Appleton Lab, Chilton OX11 0QX, U.K.

Ⓢ *Supporting Information*

ABSTRACT: We have synthesized members of an isostructural solid solution series $K_xBa_{1-x}O_{2-\delta}$ ($x < 0.41$, $\delta < 0.11$) containing mixed-valent dioxygen anions. Synthesis in liquid ammonia solution allows a continuous range of compounds to be prepared. X-ray and neutron diffraction show that $K_xBa_{1-x}O_{2-\delta}$ adopts the tetragonal rocksalt-derived structure of the end members KO_2 and BaO_2, without any structural phase transition down to 5 K, the lowest temperature studied here. We identify four oxygen−oxygen stretching modes above 750 cm^{-1} in the measured Raman spectra, unlike the spectra of KO_2 and BaO_2 which both contain just a single mode. We use density functional theory calculations to show that the stretching modes in $K_xBa_{1-x}O_{2-\delta}$ arise from in-phase and anti-phase coupling of the stretching of nearest-neighbor oxygen dimers when the valence state of the dimers lies between −1 and −2 because of mixed cation coordination. This coupling is a direct signature of a novel type of anionogenic mixed valency.

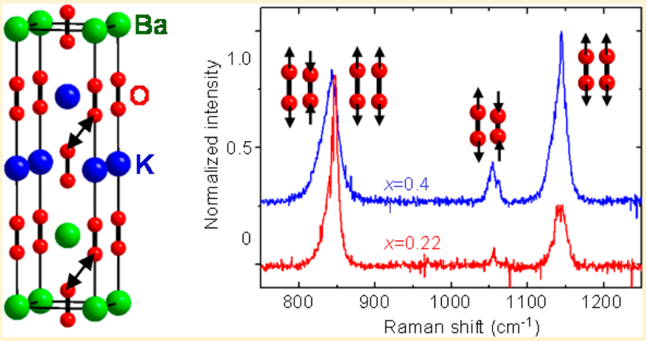

■ INTRODUCTION

The scientific and technological potential of materials in which magnetism arises from p-electrons has been much less explored than those containing magnetic d- or f-block species. This is largely due to the relative scarcity of such materials; p-electrons tend to be paired in covalent bonds. Nevertheless, in recent years an increasing number of p-electron (often carbon-based) magnetic materials have been reported.[1−8] The larger delocalization of p-electrons compared to d- or f-electrons and the low spin−orbit coupling of 2p systems is likely to yield novel physical properties, evidenced by phenomena such as spin-polarized transport in graphene.[9]

The magnetism in many p-electron systems is defect-based and is thus difficult to control and study systematically.[10,11] In contrast, dioxygen molecules carry an intrinsic magnetic moment and can thus be used as convenient building blocks to construct model systems that exhibit p-electron magnetism in an ordered, crystalline environment. The complex temperature−pressure phase diagram of diatomic molecular oxygen, which contains two unpaired electrons in doubly degenerate antibonding π^* molecular orbitals, has been studied in detail and contains a number of different antiferromagnetic (AFM) phases.[12,13] Two species of dioxygen anions also exist. The magnetic superoxide anion is formed by adding one electron to molecular O_2 and is stabilized by alkali metal cations (A) to give crystalline salts with the composition AO_2; AFM order is also widely found in these materials.[14] The nonmagnetic peroxide anion is formed by the addition of another electron to fill the π^* orbitals and is stabilized in crystalline form by both alkali and alkaline-earth (AE) cations to give compounds with the compositions AO and AEO_2, respectively.

The incorporation of both superoxide and peroxide in the same crystalline solid gives rise to the intriguing possibility of magnetic, anionogenic mixed-valent systems. By analogy with mixed-valent transition metal oxides such as the "colossal magnetoresistance" manganites,[15] this gives the prospect of novel compounds with a rich variety of physical properties that can be controlled by the filling level of the π^* orbitals.[16] It should also be noted that the orbital degeneracy of the superoxide anion leads to strong spin−lattice coupling,[17] in similar fashion to Mn^{3+}. However, the potential of mixed-valent dioxygen systems has been little studied. One approach toward obtaining such systems is to vary the oxygen content in the AO−AO_2 phase diagram. The phases in this category that have been identified and characterized thus far are $RbO_{1.5}$,[18] $CsO_{1.5}$,[19] and $RbO_{1.72}$.[20] All three compounds are insulators despite $RbO_{1.5}$ and $CsO_{1.5}$ being black in color, hinting at a different electronic structure to AO and AO_2, which are always white or pale yellow. All three compounds exhibit varying degrees of spin-glass-like behavior at low temperature, with AFM interactions dominant. $RbO_{1.5}$ is predicted to reach a half-

Received: October 2, 2013
Published: December 11, 2013

metallic ferromagnetic (FM) state at high pressure.[21] In $RbO_{1.72}$ FM interactions were observed experimentally, probably within small clusters. An alternative approach to mixed valency is suggested by the 1951 paper of Seyb and Kleinberg,[22] which reports the synthesis of a brown polycrystalline material with composition K_2BaO_6. Although not studied further to the best of our knowledge, this compound should also have nonintegral filling of the π^* orbitals, induced by the mixture of monovalent K^+ and divalent Ba^{2+} cations. Here we show that K^+ and Ba^{2+} can be combined to form a continuous solid solution series $K_xBa_{1-x}O_2$ that contains dioxygen anions with significant mixed-valent character.

■ EXPERIMENTAL SECTION

An exchange reaction was carried out between stoichiometric amounts of $Ba(NO_3)_2$ (Alfa Aesar, 95.5%) and KO_2 (Sigma Aldrich, 99.99%) in a glass round-bottomed flask connected to a vacuum line, using a method based on that reported by Seyb and Kleinberg.[22] Before commencing the synthesis, the flask was dried thoroughly by heating at 300 °C to remove adsorbed moisture. Approximately 100 mL of liquid NH_3 was condensed into the flask, the temperature of which was held constant between −40 °C and −60 °C using an ethanol bath containing an immersion cooler. The solution was continually stirred using a magnetic stirrer. A dark brown precipitate of $K_xBa_{1-x}O_2$ was gradually formed together with KNO_3 as a byproduct:

$$(2-x)KO_2 + (1-x)Ba(NO_3)_2 \rightarrow K_xBa_{1-x}(O_2^{\,-})_x(O_2^{\,2-})_{1-x} + (2-2x)KNO_3 + (1-x)O_2$$

Despite the evolution of O_2 gas in the reaction, it was found that a continuous external supply of dry O_2 (99.999%) was necessary; a partial pressure of 550 mmHg was maintained by pumping. After 30 min the reaction mixture was transferred to a U-shaped glass vessel with a filter in one arm; this vessel was attached to the vacuum line at both ends. The soluble KNO_3 byproduct was removed from the reaction mixture by washing three to four times with excess liquid NH_3, which was pulled through the filter by applying a vacuum. The moisture- and CO_2-sensitive products that were isolated by the filter were then dried in vacuum, upon which the color changed to a light tan as previously reported.[22] The samples were stored by sealing in Pyrex NMR tubes under a dry nitrogen atmosphere.

X-ray powder diffraction (XRPD, see below) showed that ~10% of $KOH{\cdot}H_2O$ impurity was always present in the final samples, as well as between 1% and 8% of KO_2 (the quantity of KO_2 was highest for the more K-rich samples). Given the precautions that were taken to exclude traces of water from the reaction environment, it is likely that $KOH{\cdot}H_2O$ originates from a side reaction between solvated KO_2 and the NH_3 solvent. It is known that hydroxides are slowly formed by the reaction of alkali metal−ammonia solutions in the presence of oxygen.[23] This possibility is supported by our observation that longer reaction times led to greater proportions of $KOH{\cdot}H_2O$. We were able to prepare $K_xBa_{1-x}O_2$ with $0.22 < x < 0.41$ by controlling the ratio of KO_2 and $Ba(NO_3)_2$ starting materials as well as the reaction temperature; the highest K-content was obtained at −40 °C, just below the boiling point of NH_3. We were unable to prepare a sample with the stoichiometry of K_2BaO_6 reported by Seyb and Kleinberg.[22] More unreacted KO_2 remained in the product when a large initial excess was used. The synthesis of $K_xBa_{1-x}O_2$ was also attempted by an analogous procedure in methylamine solvent instead of NH_3 with the aim of minimizing the side reaction, but only samples with $x < 0.25$ could be obtained by this method. The composition is likely influenced by the lower solubility of $Ba(NO_3)_2$ and KO_2 in methylamine relative to NH_3.

XRPD measurements were performed using a Huber G670 Guinier camera system operating with Cu $K_{\alpha 1}$ radiation selected by a Ge (111) monochromator. The samples were mounted in a nitrogen-filled glovebox by sandwiching the powder between two sheets of Mylar film that were clamped in place using a metal ring. The sample chamber was evacuated throughout the measurement and no signs of decomposition were seen. Temperature control was achieved using a closed-cycle refrigerator. Neutron powder diffraction (NPD) data were collected on the GEM diffractometer at the ISIS facility. Samples of mass ~0.3 g were sealed inside evacuated quartz tubes, which were in turn placed inside vanadium cans of 6 mm diameter. Data were collected down to 5 K using a helium-cooled cryostat. Structural refinements were carried out using the GSAS[24] software suite for both the XRPD and NPD data.

The overall K:Ba ratio in our samples was determined using inductively coupled plasma (ICP) analysis combined with optical emission spectrometry. The value of x in the $K_xBa_{1-x}O_2$ phase was then calculated by taking into account the percentages of $KOH{\cdot}H_2O$ impurity and unreacted KO_2 in the samples, as estimated by XRPD. Because of large uncertainties in these phase fractions (the sample peaks were very broad and overlapped strongly with many of the impurity peaks), the compositions x have experimental uncertainties of approximately ±0.05. In this paper we present results of measurements on two representative samples with compositions $K_{0.22}Ba_{0.78}O_2$ and $K_{0.41}Ba_{0.59}O_2$.

Raman spectra were measured using the backscattering configuration on samples contained in sealed, evacuated 5 mm Pyrex NMR tubes using a liquid nitrogen-cooled charged coupled device (CCD) connected to a three-grating micro-Raman spectrometer (T64000 Jobin Yvon). The sample was excited using a 532 nm semiconductor laser (VERDI) focused to an area of 50 μm^2. The resolution of this setup was ±1 cm^{-1}.

Phonon spectra were calculated from first principles using density-functional theory (DFT) with the PW91 generalized gradient approximation.[25] The projector augmented plane wave method was employed,[26,27] as implemented in the Vienna Ab Initio Simulation Package (VASP).[28−31] The core levels, which were kept frozen during the calculations, consisted of orbitals up to and including the 2p levels for K, the 4d level for Ba, and the 1s level for O. The kinetic energy cutoff was 400 eV and the experimentally determined lattice parameters were used. Here we report FM and metallic solutions unless otherwise specified. The Brillouin-zone integrations used a Γ-centered k-mesh ($10 \times 10 \times 6$) for the tetragonal unit cell determined by XRPD and NPD (see below); supercells were also constructed and employed a mesh of identical density. After relaxation of the atomic positions, selected atoms were displaced by ±0.015 Å to ±0.03 Å along the three independent axis directions (this technique was used to ensure that the force constant matrix expresses the proportionality between forces and displacements), and the corresponding forces were calculated via the Hellmann−Feynman theorem. From the calculated forces and displacements, the force-constants were obtained. Finally the phonon frequencies were obtained by diagonalization of the dynamical matrix.[32] Because only the vibrations in the center of the Brillouin zone can be detected experimentally, the calculations were limited to modes at the Γ-point (the $k = 0$ limit).

■ RESULTS AND DISCUSSION

A. X-ray and Neutron Powder Diffraction. Our XRPD and NPD data showed that $K_xBa_{1-x}O_2$ with $0.22 < x < 0.41$ adopts the body-centered tetragonal CaC_2 structure type with space group $I4/mmm$ from room temperature down to 5 K (Figure 1a), which is isostructural with the end members of the series BaO_2 and KO_2. The dioxygen anions are 6-fold coordinated by Ba/K cations to form octahedra that are strongly elongated along the c-direction. There were no unindexed peaks in the diffraction patterns; thus there is no evidence for any supercell due to Ba/K cation ordering. Rietveld refinements of the structure were carried out using fixed Ba/K ratios as determined by ICP analysis. The oxygen z-coordinate (site 4e, coordinates 0,0,z) and site occupancy were determined using NPD data collected on the $x = 0.22$ and $x = 0.41$ samples. The $x = 0.22$ sample had an oxygen deficiency of ~5.5% (Table 1), which is consistent with a previous report on

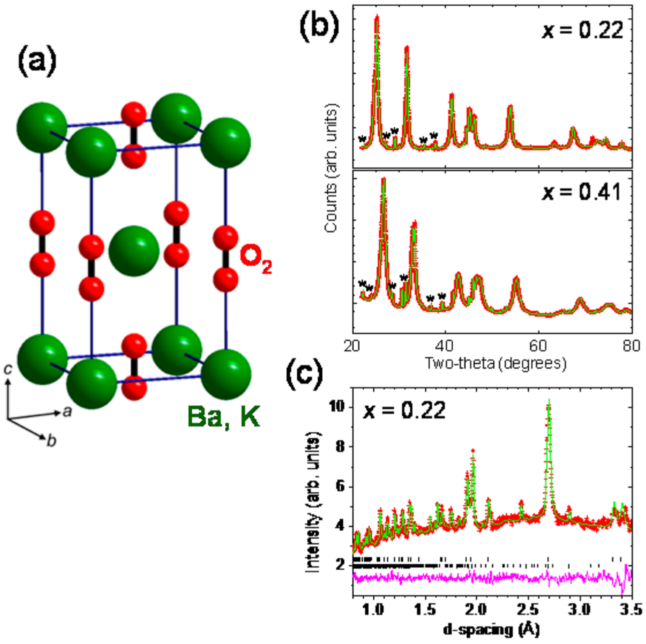

Figure 1. (a) Crystal structure of $K_xBa_{1-x}O_{2-\delta}$. (b) Observed (red data points) and calculated (green line) room temperature XRPD profiles for $x = 0.22$ and $x = 0.41$. Peaks belonging to the $KOH{\cdot}H_2O$ impurity are indicated by *. (c) Observed (red data points), calculated (green line), and difference (pink line) NPD profiles at 10 K for $x = 0.22$. Upper and lower rows of tick marks correspond to $K_xBa_{1-x}O_{2-\delta}$ and $KOH{\cdot}H_2O$, respectively.

BaO_{2-x}.[33] Using the 5 K NPD data, the refined oxygen deficiency for $x = 0.41$ was zero within a large experimental uncertainty; the occupancy could not be reliably determined from the 300 K data because of a large degree of correlation with the isotropic displacement factor. Nevertheless, the samples will hereafter be referred to as $K_xBa_{1-x}O_{2-\delta}$. The O−O bond lengths for both compounds were intermediate between those reported for BaO_{2-x} (∼1.48 Å)[33] and KO_2 (1.28 Å),[34] as shown in Table 1. The decrease in bond length with K-doping is consistent with the corresponding expected increase in bond order.

Although KO_2 is known to undergo a series of structural phase transitions below room temperature involving reorientations of the dioxygen anions, driven both by Jahn−Teller and magnetogyration effects,[35,36] our data did not indicate any phase transition in $K_xBa_{1-x}O_{2-\delta}$ down to 5 K. We note that the isotropic oxygen displacement factors of $x = 0.41$ were much larger than $x = 0.22$, which suggests that locally the anions might not be aligned perfectly parallel to *c* as imposed by *I*4/*mmm* symmetry.

The XRD and NPD peaks were much broader than the instrumental resolution; furthermore, the peak widths increased with *x*. The high degree of peak overlap prevented an accurate size/strain analysis, but applying the Scherrer formula to the width of the 112 peak (the only well resolved $K_xBa_{1-x}O_{2-\delta}$ single peak in the patterns) suggested a crystallite size of the order 15−30 nm for $x = 0.41$. A significant contribution to the peak broadening could also arise from strain if the samples are inhomogeneous with respect to the Ba/K distribution, for example if the cations are locally ordered. Annealing at 100 °C resulted in narrower diffraction peaks but also in the appearance of weak extra peaks that could not be indexed in terms of either a supercell or any known impurity phase. To ensure as high sample quality as possible in terms of purity, the samples discussed here were not annealed.

B. Raman Spectroscopy. Figure 2 shows the room temperature Raman spectra of $K_{0.22}Ba_{0.78}O_{2-\delta}$ and $K_{0.41}Ba_{0.59}O_{2-\delta}$. For each sample three peaks A, B, and C were observed in the region between 800 and 1200 cm^{-1}, the range in which O−O stretching modes are expected to appear. Peaks A and C at ∼840 cm^{-1} and ∼1140 cm^{-1} are close to the previously reported O−O stretching modes of the O_2^{2-} and O_2^{-} species (843−851 cm^{-1} for BaO_{2-x} depending on *x*[33] and 1141−1143 cm^{-1} for KO_2[37,38]). On closer inspection both peaks could best be fitted using pairs of Lorentzian functions, except for the ∼1140 cm^{-1} peak of $x = 0.22$ which required only one broad Lorenztian. A third peak B at ∼1055 cm^{-1} is also apparent; no O−O stretching mode close to this frequency has been reported in the literature. Although the C−O stretching frequency of the carbonate anion is found here,[33] no evidence of carbonates was found in any of the XRPD or

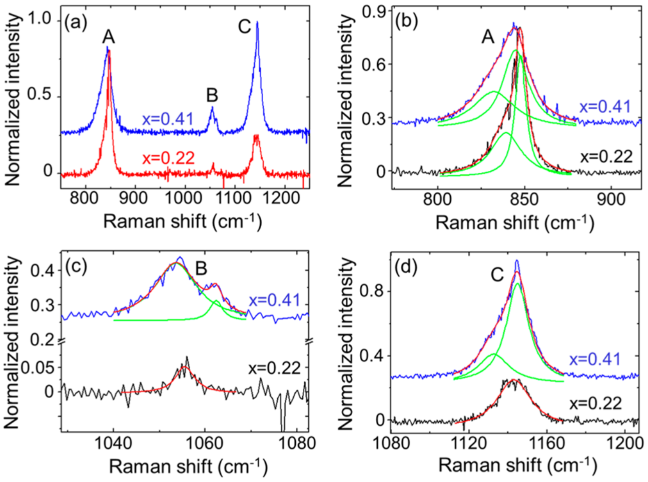

Figure 2. Raman spectra of $K_xBa_{1-x}O_{2-\delta}$ ($x = 0.22$ and 0.41) showing (a) the frequency range in which the O−O stretching modes are found and (b)−(d) close-up views of features A, B, and C, where green lines show Lorentzian fits to individual peaks within doublets and red lines show the overall fit to a doublet.

Table 1. Refined Structural Parameters of $K_xBa_{1-x}O_{2-\delta}$[a]

	a (Å)	*c* (Å)	O *z*	O−O (Å)	*δ*	$U_{Ba/K}$ (Å^2)	U_O (Å^2)
x = 0.22, 290 K	3.8259(2)	6.8307(7)	0.3929(2)	1.463(3)	0.14(4)	0.0089(18)	0.0062(11)
x = 0.22, 10 K	3.8090(2)	6.8076(7)	0.3932(3)	1.455(3)	0.08(4)	−0.0008(16)	0.0050(13)
x = 0.41, 290 K	3.8319(5)	6.8203(11)	0.3945(4)	1.439(6)		0.0030(18)	0.031(3)
x = 0.41, 5 K	3.8116(7)	6.7967(17)	0.3965(7)	1.407(10)	−0.01(10)	0.005(3)	0.046(6)

[a] Space group *I*4/*mmm*, K/Ba at 2*a* (0,0,0), O at 4*e* (0,0,*z*). Table lists unit cell parameters, oxygen *z*-coordinates, O−O bond lengths, oxygen deficiency *δ*, isotropic displacement factors $U_{Ba/K}$ and U_O as determined by NPD.

Table 2. Peak Positions and Widths of O−O Stretching Modes

	peak A		peak B		peak C	
	position (cm^{-1})	width (cm^{-1})	position (cm^{-1})	width (cm^{-1})	position (cm^{-1})	width (cm^{-1})
BaO_2	842.6(8)	4.9(5)				
KO_2					1142.8(6)	4.3(4)
$K_{0.22}Ba_{0.78}O_{2-\delta}$	839.1(1.4)	21(3)	1054.2(1)	8.82(6)	1142.9(2)	21.7(1.1)
	847.6(1)	7.5(6)				
$K_{0.41}Ba_{0.59}O_{2-\delta}$	833(2)	15(6)	1056.5(1)	13.26(1)	1132.6(1.0)	13.9(9)
	844.8(9)	13(2)			1144.8(2)	20(3)

NPD patterns, and this peak was absent in Raman spectra of KO_2 and BaO_2 samples stored under identical conditions. The origin of this peak will be discussed in detail below. The fitted peak parameters of BaO_2, KO_2, and $K_xBa_{1-x}O_{2-\delta}$ are summarized in Table 2. All three $K_xBa_{1-x}O_{2-\delta}$ peaks are significantly broader than the O−O stretching peaks of BaO_2 and KO_2, probably reflecting variation in the local chemical environment of the dioxygen anions due to cation disorder. Although the peaks have been fitted with either one or two Lorentzians, as discussed below they should probably be envisaged as the superposition of many narrower peaks covering a range of frequencies because many different local coordinations of Ba/K are possible.

DFT calculations were performed to better understand the Raman spectra in Figure 2. We considered oxygen dimers with a first octahedral coordination sphere of six mixed Ba^{2+} and K^+ cations, where the molecular axis of the dimers is along the *c*-direction. In total, there are 16 possible combinations of cations for a given dimer, not including coordinations of six Ba^{2+} or six K^+. For each combination, a larger unit cell was constructed to include the first coordination sphere of one dimer. The dimer under investigation was relaxed along the *c*-axis of the body-centered tetragonal cell. The frequency ν of the corresponding Raman-active O−O stretching mode was then calculated; values for each possible coordination are listed in Table S1 of the Supporting Information. The frequencies cover the range from ν = 853 cm^{-1} for Ba-rich coordination to ν = 1098 cm^{-1} for K-rich coordination. The coordination in the *ab* plane has a stronger influence on ν than that along the *c*-direction, especially for dimers with a higher K-coordination. For example, a dimer coordinated by one axial Ba^{2+} and five K^+ gives the highest ν of 1098 cm^{-1}; moving the Ba^{2+} to an equatorial position reduces ν to 973 cm^{-1}. This trend is not as pronounced for Ba-rich coordinations, where ν varies less.

The local cation coordination of a dimer determines its valence state. The ground state of a dimer can be described by a linear combination of the ground states of O_2^- and O_2^{2-}: $O_2^{y-} = (1-\alpha^2)^{1/2}O_2^- + \alpha O_2^{2-}$, where $y-$ is the nominal valence state of the dimer and α ($0 < \alpha < 1$) represents the valence mixing. The value of α is close to 1 for Ba^{2+}-rich coordination, and for K^+-rich coordination α is close to zero. We demonstrate here that Raman spectra represent a useful probe of to what degree these mixed-valent anions interact with each other. Indeed, by considering isolated dimers only, the calculated stretching frequencies in Supporting Information, Table S1 cannot account for the three experimental peaks observed at ~840, 1055, and 1140 cm^{-1}. Instead, we propose that the entire spectrum can be interpreted by including the effect of coupling the vibrations of adjacent dimers. The *I*4/*mmm* unit cell of $K_xBa_{1-x}O_{2-\delta}$ contains six atoms: two cations and two oxygen dimers. The stretching of the two dimers can either be in-phase or anti-phase, and we must consider both cases for couplings between nearest neighbors, which can also have different K/Ba environments. We note that coupling of a dimer coordinated by six K^+ to a nearest-neighbor coordinated by six Ba^{2+} is not possible because the octahedra share edges. However, coupling between dimers with any other combination of coordinations is possible. To gain insight into the effect of this coupling on the stretching frequencies, we performed a series of representative calculations on $K_{0.5}Ba_{0.5}O_2$ using unit cells doubled either in the *ab* plane or in the *c*-direction, as shown in Figure 3. When the interaction between two specific dimers was calculated in cases 1−6 below, we performed a separate phonon calculation for each case where we kept all other atoms in the cell frozen.

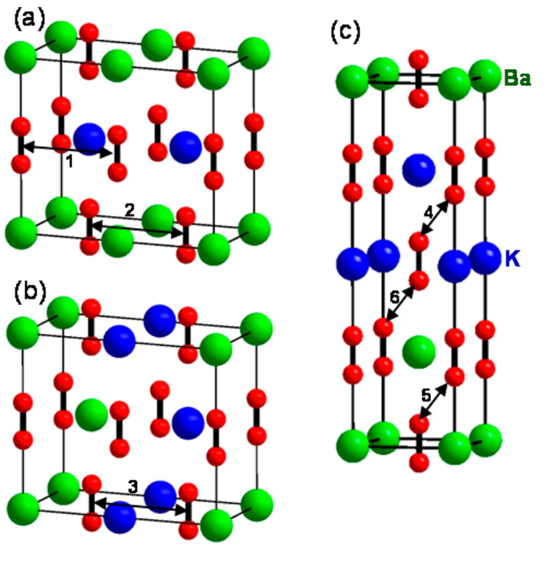

Figure 3. Supercells used for phonon calculations of $K_{0.5}Ba_{0.5}O_2$ with (a), (b) intralayer coupling between oxygen dimers in the *ab* plane and (c) interlayer coupling. Labels 1−6 correspond to the coupling cases described in the text and in Table 3.

First, three representative cases were studied in which neighboring dimers are coupled in the *ab* plane (i.e., intralayer coupling; the supercells used are shown in Figures 3a and b). The calculated frequencies are shown in Table 3. Analyzing the motion of the atoms in these calculations, we found that the higher frequency mode in each of cases 1 to 3 corresponds to in-phase stretching and the lower frequency corresponds to anti-phase stretching.

Three more representative cases were studied in which neighboring dimers couple along the [111] direction of the smaller *I*4/*mmm* cell (i.e., interlayer coupling, the supercell used is shown in Figure 3c). The calculated frequencies are also listed in Table 3. Similar to intralayer coupling, in cases 4 and 5 the higher and lower frequencies correspond to in-phase and anti-phase stretching, respectively. The difference between in-

Table 3. Frequencies of O−O Stretching Modes for Coupled Dimers A and B[a]

O_2 dimer coordinations and interactions				calculated frequencies (cm^{-1})			
case	dimer A	dimer B	interaction	with coupling		no coupling	
1	2Ba, 4K	2Ba, 4K	intralayer (Figure 3a)	995	1079		1079
2	4Ba, 2K	4Ba, 2K	intralayer (Figure 3a)	852	886		886
3	2Ba, 4K	4Ba, 2K	intralayer (Figure 3b)	893	970	901	938
4	1Ba, 5K	1Ba, 5K	interlayer (Figure 3c)	1068	1134		1098
5	5Ba, 1K	5Ba, 1K	interlayer (Figure 3c)	868	887		879
6	1Ba, 5K	5Ba, 1K	interlayer (Figure 3c)	877	1103	879	1098

[a] Cases 1−6 correspond to the dimer couplings labeled in Figures 3a-c. The second and third columns give the cation coordination of each dimer in the coupled pair. Calculated frequencies are given for coupled and isolated dimers.

phase and anti-phase stretching frequencies is much larger for coupling between the superoxide-like dimers in case 4 than for the peroxide-like dimers in case 5. The coupling between superoxide-like and peroxide-like dimers in case 6 has a negligible effect on the frequencies. This is in contrast to the intralayer coupling of “oppositely” coordinated dimers in case 3, which has a much greater effect on the frequencies because of the more mixed-valent character of the 4:2 and 2:4 coordinated dimers [in case 6, the dimer coordinations are 5:1 and 1:5].

Finally, we performed three phonon calculations based on ordered structures with compositions $K_{0.25}Ba_{0.75}O_2$, $K_{0.5}Ba_{0.5}O_2$, and $K_{0.75}Ba_{0.25}O_2$ (note that in these calculations all dimers were allowed to interact). Details are given in the Supporting Information. We assumed that the magnetic moments of dimers within each K−O layer (in the *ab*-plane) were coupled ferromagnetically, as reported in the literature for KO_2.[39] For $K_{0.25}Ba_{0.75}O_2$ and $K_{0.75}Ba_{0.25}O_2$ the calculated and experimentally observed frequencies differed significantly. However, a good match with the experimental frequencies of both the x = 0.22 and x = 0.41 samples (Figure 2) was obtained for $K_{0.5}Ba_{0.5}O_2$. The results are summarized in Table 4. The highest calculated frequency of 1134 cm^{-1} is close to the experimental value of ~1140 cm^{-1}. Similarly, the calculated 1068 cm^{-1} mode is close to the experimental peak at 1055 cm^{-1}. The 887 cm^{-1} and 868 cm^{-1} modes are consistent with the broad experimental doublet centered at ~840 cm^{-1}. We note that the supercell used for $K_{0.5}Ba_{0.5}O_2$ (Figure 3c) contains only one dimer per layer in the *ab*-plane; thus intralayer dimer coupling is neglected in our calculation. Our justification for this assumption is outlined in the Supporting Information; essentially, intralayer coupling is very weak because of the longer distance between dimers (~3.86 Å) compared to the interplane distance (~3.40 Å).

Table 4. Calculated and Observed O−O Stretching Mode Frequencies for $K_{0.5}Ba_{0.5}O_2$ Supercell in Figure 3c

dimer coordination		calculated (observed) frequency (cm^{-1})	
dimer A	dimer B	in-phase stretching	anti-phase stretching
1Ba, 5K	1Ba, 5K	1134 (1140)	1068 (1055)
5Ba, 1K	5Ba, 1K	887 (840)	868 (840)

Although based on simple ordered structural models, the phonon calculations above give us useful information on the Raman spectra of our samples. The fact that only the phonon calculation on $K_{0.5}Ba_{0.5}O_2$ gives reasonable agreement with experiment implies that a structure with a fair degree of K^+/Ba^{2+} order is formed, probably on length scales more local than can be probed by standard diffraction methods. When the concentration of K^+ in the sample is much lower than 50%, the structure is likely inhomogeneous with local regions of cation order similar to the supercell in Figure 3c, and other regions where the dimers are coordinated mainly by Ba^{2+}. This is consistent with the observation that the two peaks centered at 1055 cm^{-1} and 1140 cm^{-1} are both weaker for x = 0.22 than for x = 0.41 (Figure 2). When the K^+ concentration approaches 50%, one may expect a greater tendency toward the cation-ordered structure. Consequently, we expect that the two peaks centered at 1055 cm^{-1} and 1140 cm^{-1} will have the strongest combined intensities at x = 0.5 in the $K_xBa_{1-x}O_{2-\delta}$ series.

Usually, only phonons at the center of the Brillouin zone (k = 0) are first-order Raman allowed because of momentum conservation, which is associated with the translational symmetry of the crystal. Introducing disorder into the lattice breaks this translational symmetry, which consequently causes the breakdown of momentum conservation and violation of the selection rules. The usual effects of disorder on the Raman spectra of crystalline materials are peak broadening and the activation of k = 0 phonons that are forbidden by the symmetry of the perfect crystal. We will first discuss the Raman spectrum of an alkali oxide crystal in which each dimer has the same cation coordination. For neighboring dimers that stretch in-phase, during the period when the bond length of the dimers increases, the polarizability of both dimers also increases with the same scaling coefficient. The total derivative of the polarizability with respect to the normal coordinate taken at the equilibrium position is then nonzero. Consequently, the in-phase stretching vibration is Raman active.[40] For anti-phase stretching, during the period when the bond length of one dimer increases and that of the other dimer decreases, the polarizability of the first dimer is increasing with the same scaling coefficient as for in-phase stretching, whereas the polarizability of the second dimer decreases with a scaling coefficient of opposite sign. The derivative of the total polarizability with respect to the normal coordinate taken at the equilibrium position is then zero (the contribution of one dimer completely cancels that of the other dimer). Consequently, the anti-phase stretching vibration is Raman inactive. However, the mixed valency that arises from the disordered distribution of Ba^{2+}/K^+ in $K_xBa_{1-x}O_{2-\delta}$ introduces random variations in the chemical environment of the dimers. The resulting Raman spectrum would then differ from that of the perfectly ordered crystal discussed above. For in-phase stretching, the polarizability of neighboring dimers will increase/decrease with the same sign but the scaling coefficients can be of different magnitude. The total derivative of the polarizability with respect to the normal coordinate taken at the equilibrium position would then be nonzero, and the in-phase stretching vibration would still be Raman active. For anti-phase stretching, the polarizability of one dimer will increase with some scaling coefficient while the polarizability of the other dimer decreases with a scaling coefficient of the opposite sign that can also be different in magnitude. The derivative of the total polarizability with respect to the normal coordinate taken at the equilibrium position would then be nonzero and this anti-phase stretching vibration would become Raman active. Thus, structural disorder due to mixed valency in $K_xBa_{1-x}O_{2-\delta}$ activates the anti-phase stretching mode that would be Raman-forbidden by the symmetry of a perfectly ordered crystal. We note that this mechanism is different to other examples of disorder-induced Raman scattering in the literature, such as in relaxor ferroelectrics where there are distinct clusters or nanoregions with lower symmetry than of the bulk material.[41] A secondary effect resulting from the surfaces of small crystallites (15−30 nm suggested by our XRPD measurements) might also help to activate the anti-phase stretching mode in $K_xBa_{1-x}O_{2-\delta}$. On the surface of the crystallites, the anti-phase stretching of adjacent dimers does not result in complete cancellation of the polarizability (Figure 4). Thus, the Raman-forbidden mode can become weakly activated. Such an effect is known for the so-called D-mode in graphite, the intensity of which scales inversely with crystallite size.[42,43] However, in $K_xBa_{1-x}O_{2-\delta}$ the effect of crystallite size is likely to be small in comparison to the influence of cation disorder.

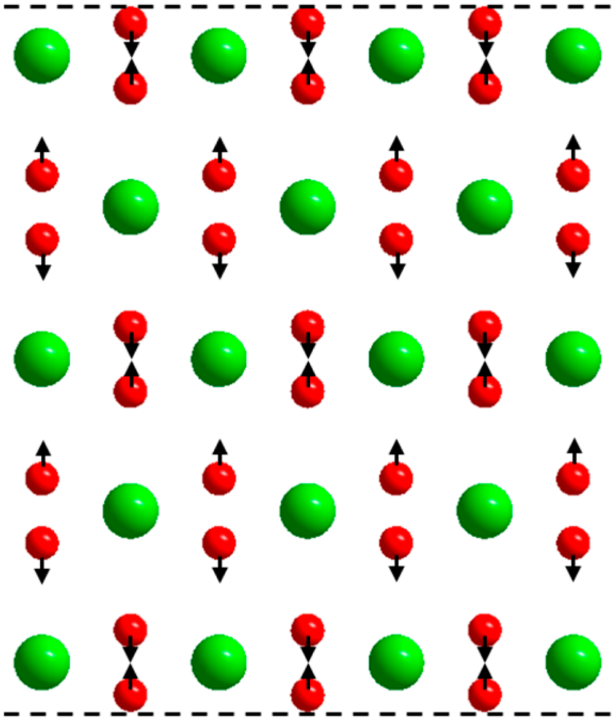

Figure 4. Schematic representation of activation of the Raman-forbidden anti-phase stretching mode for a finite-sized crystallite of $K_xBa_{1-x}O_{2-\delta}$ with upper and lower surfaces indicated by dashed lines. Green and red spheres represent K/Ba and O, respectively. Arrows represent stretching/compression of O−O bonds.

Mixed-valent transition metal based compounds have been widely studied. Robin and Day[44,45] classified mixed-valent compounds into three categories according to the extent of the electronic interaction between redox units. At present it is unclear to which category $K_xBa_{1-x}O_{2-\delta}$ should be assigned; our attempts to measure the electrical conductivity were unsuccessful as we were unable to prepare dense enough pellets below the sample decomposition temperature of ~100 °C. Magnetization measurements showed behavior characteristic of spin glasses for all samples and are reported elsewhere.[46] Nevertheless, our interpretation of the Raman spectra of $K_xBa_{1-x}O_{2-\delta}$ requires a considerable degree of coupling between neighboring dioxygen dimers.

Finally, we briefly comment on the other nominally mixed-valent alkali oxides. The Raman spectra of $RbO_{1.5}$ and $CsO_{1.5}$[19] show only two peaks in the O−O stretching frequency range, which are close to the expected frequencies of peroxide and superoxide anions. The absence of any intermediate frequency peaks suggests that no significant coupling between the oxygen dimers in $RbO_{1.5}$ and $CsO_{1.5}$ occurs. This is supported by the observation of the same two peaks in the vibrational spectrum of $RbO_{1.5}$ obtained by inelastic neutron scattering,[47] a technique that unlike Raman spectroscopy has no selection rules[48] and for which anti-phase stretching modes would always be visible. Therefore, the dioxygen anions in $RbO_{1.5}$ and $CsO_{1.5}$ likely retain discrete 1− and 2− charges, and they can be considered as anionogenic charge-ordered materials. The Raman spectrum of $RbO_{1.72}$ contains one strong stretching mode at the frequency of superoxide and one very weak mode at the frequency of peroxide.[20] Here the stoichiometry does not allow any obvious type of charge order, but no intermediate frequency modes suggestive of mixed-valent dimer coupling were observed. However, this might be because all the dioxygen anions are identically coordinated by six Rb^+ cations, resulting in the anti-phase stretching mode of coupled dimers being Raman forbidden.

■ CONCLUSION

We have synthesized a continuous solid solution series of anionogenic mixed-valent materials with formula $K_xBa_{1-x}O_{2-\delta}$ ($x < 0.41$). All materials are isostructural with the end members $BaO_{2-\delta}$ and KO_2. The Raman spectra contain an O−O stretching mode centered at ~ 1055 cm^{-1} that is intermediate in frequency between those of superoxide and peroxide anions and has not previously been observed in related materials with dioxygen anions. We have shown that this mode arises from coupling between neighboring oxygen dimers when the valence state of the anions lies between −1 and −2, and is thus a direct signature of a novel type of anionogenic mixed valency. We expect that a new family of materials based on mixed-valent dioxygen anions combined with alkali and alkaline earth cations awaits discovery, with as yet unknown physical properties.

■ ASSOCIATED CONTENT

Ⓢ Supporting Information

Further details of phonon calculations on $K_xBa_{1-x}O_2$, BaO_2, and KO_2. This material is available free of charge via the Internet at http://pubs.acs.org.

■ AUTHOR INFORMATION

Corresponding Author

*E-mail: g.r.blake@rug.nl.

Present Addresses

⊥Max Planck Institute for Chemical Physics of Solids, Nöthnitzer Str. 40, 01187 Dresden, Germany.
⊗Institute of Physics II, University of Cologne, Zülpicher Str. 77, 50937 Cologne, Germany.

Author Contributions

‖S.G. and B.Z. contributed equally.

Notes

The authors declare no competing financial interest.

■ ACKNOWLEDGMENTS

We thank J. Baas for technical support. This work is part of the research program of the Foundation for Fundamental Research on Matter (FOM) and of Chemical Sciences (CW), which are financially supported by The Netherlands Organization for Scientific Research (NWO).

■ REFERENCES

(1) Volnianska, O.; Boguslawski, P. *J. Phys.: Condens. Matter* **2010**, *22*, 073202.
(2) Coey, J. M. D. *Curr. Opin. Solid State Mater. Sci.* **2006**, *10*, 83−92.
(3) Sundaresan, A.; Rao, C. N. R. *Nano Today* **2009**, *4*, 96−106.
(4) Yang, C. -K. *Appl. Phys. Lett.* **2008**, *92*, 033103.
(5) Ohldag, H.; Tyliszczak, T.; Höhne, R.; Spemann, D.; Esquinazi, P.; Ungureanu, M.; Butz, T. *Phys. Rev. Lett.* **2007**, *98*, 187204.
(6) Narymbetov, B.; Omerzu, A.; Kabanov, V. V.; Tokumoto, M.; Kobayashi, H.; Mihailovic, D. *Nature* **2000**, *407*, 883−885.
(7) McCreary, K. M.; Swartz, A. G.; Han, W.; Fabian, J.; Kawakami, R. K. *Phys. Rev. Lett.* **2012**, *109*, 186604.
(8) Ning, G.; Xu, C.; Hao, L.; Kazakova, O.; Fan, Z.; Wang, H.; Wang, K.; Gao, J.; Qian, W.; Wei, F. *Carbon* **2013**, *51*, 390−396.
(9) Tombros, N.; Jozsa, C.; Popinciuc, M.; Jonkman, H. T.; van Wees, B. J. *Nature* **2007**, *448*, 571−574.
(10) Zunger, A.; Lany, S.; Raebiger, H. *Physics* **2010**, *3*, 53.
(11) Kuzemsky, A. L. *Int. J. Mod. Phys. B* **2013**, *27*, 1330007.
(12) Freiman, Yu. A.; Jodl, H. J. *Phys. Rep.* **2004**, *401*, 1−228.
(13) Meier, R. J.; Helmholdt, R. B. *Phys. Rev. B* **1984**, *29*, 1387−1393.
(14) Labhart, M.; Raoux, D.; Känzig, W.; Bösch, M. A. *Phys. Rev. B* **1979**, *20*, 53−70.
(15) Kim, K. H.; Uehara, M.; Kiryukhin, V.; Cheong, S. -W. In *Colossal Magnetoresistive Manganites*; Chatterji, T., Ed.; Kluwer Academic Publishers: Dordrecht, The Netherlands, 2002.
(16) Attema, J. J.; de Wijs, G. A.; Blake, G. R.; de Groot, R. A. *J. Am. Chem. Soc.* **2005**, *127*, 16325−16328.
(17) Solovyev, I. *New J. Phys.* **2008**, *10*, 013035.
(18) Winterlik, J.; Fecher, G. H.; Jenkins, C. A.; Felser, C.; Mühle, C.; Doll, K.; Jansen, M.; Sandratskii, L. M.; Kübler, J. *Phys. Rev. Lett.* **2009**, *102*, 016401.
(19) Winterlik, J.; Fecher, G. H.; Jenkins, C. A.; Medvedev, S.; Felser, C.; Kübler, J.; Mühle, C.; Doll, K.; Jansen, M.; Palasyuk, T.; Trojan, I.; Eremets, M. I.; Emmerling, F. *Phys. Rev. B* **2009**, *79*, 214410.
(20) Riyadi, S.; Giriyapura, S.; de Groot, R. A.; Caretta, A.; van Loosdrecht, P. H. M.; Palstra, T. T. M.; Blake, G. R. *Chem. Mater.* **2011**, *23*, 1578−1586.
(21) Naghavi, S.; Chadov, S.; Felser, C.; Fecher, G. H.; Kübler, J.; Doll, K.; Jansen, M. *Phys. Rev. B* **2012**, *85*, 205125.
(22) Seyb, E.; Kleinberg, J. *J. Am. Chem. Soc.* **1951**, *73*, 2308−2309.
(23) Watt, G. W. *Chem. Rev.* **1950**, *46*, 289−315.
(24) Larson, A. C.; von Dreele, R. B. *General Structure Analysis System* (*GSAS*, Los Alamos National Laboratory Report LAUR 86-748; Los Alamos National Laboratory: Los Alamos, NM, 2004.
(25) Perdew, J. P.; Chevary, J. A.; Vosko, S. H.; Jackson, K. A.; Pederson, M. R.; Singh, D. J.; Fiolhais, C. *Phys. Rev. B* **1992**, *46*, 6671−6687.
(26) Blöchl, P. E. *Phys. Rev. B* **1994**, *50*, 17953−17979.
(27) Kresse, G.; Joubert, D. *Phys. Rev. B* **1999**, *59*, 1758−1775.
(28) Kresse, G.; Hafner, J. *Phys. Rev. B* **1993**, *47*, 558−561.
(29) Kresse, G.; Hafner, J. *Phys. Rev. B* **1994**, *49*, 14251−14269.
(30) Kresse, G.; Furthmüller, J. *Comput. Mater. Sci.* **1996**, *6*, 15−50.
(31) Kresse, G.; Furthmüller, J. *Phys. Rev. B* **1996**, *54*, 11169−11186.
(32) Kresse, G.; Furthmüller, J.; Hafner, J. *Europhys. Lett.* **1995**, *32*, 729−734.
(33) Königstein, M. *J. Solid State Chem.* **1999**, *147*, 478−484.
(34) Ziegler, M.; Rosenfeld, M.; Känzig, W.; Fischer, P. *Helv. Phys. Acta* **1976**, *49*, 57−90.
(35) Bösch, M. A.; Lines, M. E.; Labhart, M. *Phys. Rev. Lett.* **1980**, *45*, 140−143.
(36) Lines, M. E.; Bösch, M. A. *Phys. Rev. B* **1981**, *23*, 263−270.
(37) Hesse, W.; Jansen, M.; Schnick, W. *Prog. Solid State Chem.* **1989**, *19*, 47−110.
(38) Bates, J. B.; Brooker, M. H.; Boyd, G. E. *Chem. Phys. Lett.* **1972**, *16*, 391−395.
(39) Smith, H. G.; Nicklow, R. M.; Raubenheimer, L. J.; Wilkinson, M. K. *J. Appl. Phys.* **1966**, *37*, 1047−1049.
(40) Long, D. A. *The Raman Effect: a Unified Treatment of the Theory of Raman Scattering by Molecules*; John Wiley & Sons, Inc.: Chichester, U.K., 2002.
(41) Torgashev, V. I.; Yuzyuk, Yu. I.; Latush, L. T.; Timonin, P. N.; Farhi, R. *Ferroelectrics* **1997**, *199*, 197−205.
(42) Tuistra, F.; Koenig, J. L. *J. Chem. Phys.* **1970**, *53*, 1126−1130.
(43) Pimenta, M. A.; Dresselhaus, G.; Dresselhaus, M. S.; Cançado, L. G.; Jorio, A.; Saito, R. *Chem. Phys. Phys. Chem.* **2007**, *9*, 1276−1291.
(44) Robin, M. B.; Day, P. *Adv. Inorg. Chem. Radiochem.* **1967**, *10*, 247−422.
(45) Day, P.; Hush, N. S.; Clark, R. J. H. *Phil. Trans. R. Soc. A* **2008**, *366*, 5−14.
(46) Giriyapura, S. Ph.D. Thesis, University of Groningen, Groningen, The Netherlands, November 2012; http://irs.ub.rug.nl/ppn/35216378X.
(47) Jansen, M.; Hagenmayer, R.; Korber, N. *C. R. Acad. Sci. Paris, Ser. IIc: Chim.* **1999**, *2*, 591−594.
(48) Hudson, B. S. *J. Phys. Chem. A* **2001**, *105*, 3949−3960.